Response to Referee#1

Thank you for your careful assessment and valuable comments. The comments and suggestions are very useful for our manuscript. We have carefully studied these comments and suggestions and made some changes in our manuscript.

Comment 1)

"To overcome these limitations" … I think especially the sensitivity to Mie scattering is not solved yet. Your temperature profiles can only be used above 5.3 km due to the contamination from aerosols. Hence, I would skip this argument in the abstract.

Response:

Thank you for this important comment. We agree that the influence of Mie scattering is not completely eliminated and that the original wording was not sufficiently precise. Following the reviewer's suggestion, we have revised the manuscript accordingly. These revisions have been made in the Abstract on Page 1, Lines 13–18 and 24–26, and Page 2, Lines 54–62.

Comment 2)

As you are addressing RB scattering research, which I think is indeed very crucial for the presented measurement technology, it might be useful to mention the first studies performed in air: https://doi.org/10.1364/AO.49.004217

Response:

Thank you for this helpful suggestion. We have added the pioneering experimental study by Witschas et al. (2010) to the Introduction when discussing early Rayleigh–Brillouin scattering measurements in air. The corresponding reference and a brief description of its contribution have been added on Page 2–3, Lines 62–64.

Comment 3)

You approximate the Fizeau transmission function, which is only a valid approach for low-Finesse systems. For high-Finesse Fizeau interferometers, a clearly asymmetric

transmission function arises, which has to be considered. I would recommend justifying your approach here.

Response:

Thank you for this valuable comment. We agree that the applicability of the Airy-function approximation should be further justified. Following McKay (Mckay, 2002), we have introduced the shape factor S and its calculation in the revised manuscript. For the developed Fizeau interferometer, the calculated shape factor is S=0.062. This value is well below the criterion of S<0.6, supporting the applicability of the Airy-function approximation to the interference fringe. The relevant definitions, calculation, reference, and discussion have been added to Page 5, Lines 136-143 while the calculated value of S and the corresponding conclusion have been added to Page 11, Lines 266–267 of the revised manuscript.

Comment 4)

In the Rayleigh-Brillouin community, your parameters "a" and "b" are usually called the dimensionless frequency "x" and the parameter "y." I think you could either use this nomenclature or, at least, briefly mention it here.

Response:

Thank you for this comment. We have revised the corresponding variables to x and y and clarified their definitions on Page 6, Lines 154-169.

Comment 5)

I think it is better to call θ the scattering angle. It would also be useful to give numbers for the shear viscosity in air (the value that you use) and for θ = 180° for lidar measurements.

Response:

Thank you for this comment. We have replaced "divergence angle" with "scattering angle" and clarified that $\theta = 180°$ for lidar backscattering measurements on Page 6, Lines 164. We have also specified the shear viscosity of air used in the calculation, $\eta = 1.846 \times 10^{-5}\ \mathrm{kg\,m^{-1}\,s^{-1}}$, which is used in the calculation of the uniformity

parameter y in the G3 model(Witschas, 2011a, b; Witschas et al., 2010), on Page 6, Line 162.

Comment 6)

It is very important to distinguish between the correct physical line-shape model by Tenti, which has no closed analytical form, and the approximation by Witschas, which is based on the superposition of three Gaussians, as you show in Eq. (8). As Witschas derived his model based on the x and y parameters, it is indeed possible to substitute these and make it dependent on p and T. However, it has to be made clear that this is the equation by Witschas and not the Tenti model.

Response:

Thank you for this important comment. We have clarified that the Tenti S6 model has no closed-form analytical expression and that Eq. (9) is the three-Gaussian analytical approximation developed by Witschas (Witschas, 2011a, b). These revisions have been made on Page 6, Lines 154-169.

Comment 7)

Can you also provide numbers for the spectral pulse width as well as the frequency stability of the laser, which are both important quantities for the applied technology?

Response:

Thank you for this valuable comment. We acknowledge that the spectral linewidth of the pulsed laser was not independently measured during the experiment. According to the manufacturer's performance report, the laser linewidth is less than 1 GHz. Importantly, the receiver transmission profile was experimentally characterized using the same pulsed laser employed for the atmospheric measurements. Therefore, the measured spectral response of the receiver inherently includes the effect of the finite laser linewidth, and this effect is consequently accounted for in the subsequent spectral analysis and retrieval.

In addition, with all other receiver parameters kept unchanged, the receiver transmission profile was independently measured using a narrow-linewidth continuous-

wave laser with a linewidth of approximately 100 kHz. Because its linewidth is negligible compared with the spectral width of the receiver, this measurement provides an approximation of the intrinsic receiver transmission function. By comparing the transmission profiles measured with the continuous-wave and pulsed lasers and performing deconvolution, the spectral linewidth of the pulsed laser was estimated to be approximately 0.67 GHz, consistent with the manufacturer-specified value of less than 1 GHz.

During the atmospheric observations on 30 June 2026, the laser frequency was continuously monitored using a HighFinesse WS8-2 wavelength meter with a frequency resolution of approximately 0.1 MHz to evaluate its frequency stability. The measured frequency fluctuations over the observation period are shown in Fig. R1.

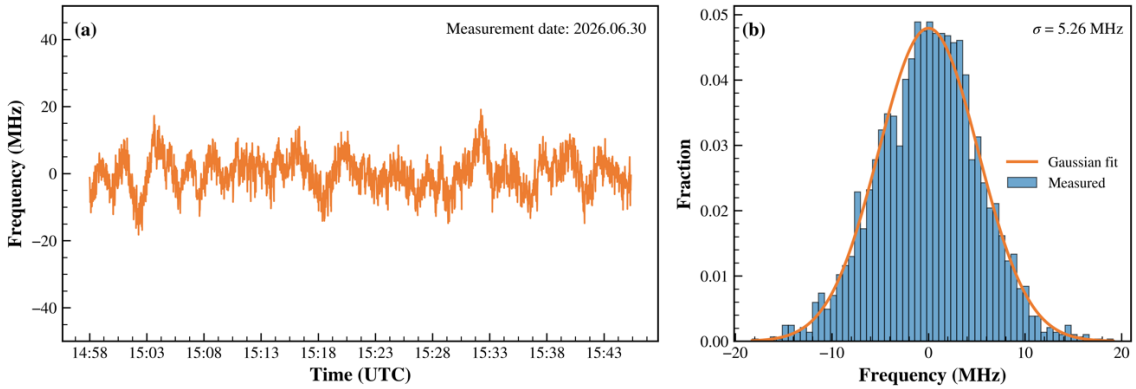


Figure R1. Laser frequency fluctuations measured by a wavelength meter during the atmospheric observation period.

The laser frequency remained stable throughout the measurement period, with a standard deviation of 5.26 MHz over the entire observation period.

Comment 8)

Using a multimode fiber should cause speckle issues in the imaged fringes. How do you deal with that? Do you use an additional fiber scrambler? Further, the larger fiber core together with the NA of 0.22 broadens the transmission fringe of the Fizeau significantly (compared to SM fiber illumination). Do you consider that? Does this cause error sources?

Response:

Thank you for this insightful comment. Yes, an additional fiber scrambler was employed after the multimode fiber to suppress speckle effects and improve the spatial uniformity of the beam incident on the Fizeau interferometer. This point has now been clarified in the revised manuscript on Page 8, Lines 189, and the fiber scrambler has also been added to the optical layout shown in Fig. 2 in manuscript to more accurately represent the actual receiver configuration.

We agree that the finite core diameter and numerical aperture (NA) of the multimode fiber introduce an angular spread in the collimated beam, which may broaden the transmission fringe of the Fizeau interferometer. In our receiver, the collected signal is coupled into a multimode fiber with a core diameter of 200 μm and an NA of 0.22. After passing through the fiber scrambler, the output beam is collimated by a lens with a diameter of 50 mm and a focal length of approximately 114 mm. The angular spread after collimation is calculated as:

$$\theta = \arctan\left(\frac{d/2}{f}\right) = \arctan\left(\frac{100\ \mu m}{114\ mm}\right) \approx 0.88\ mrad$$

The divergence half-angle is approximately 0.88 mrad. To quantitatively evaluate the influence of this finite beam divergence on the transmission characteristics of the Fizeau interferometer, the transmission profiles for divergence half-angles of 0 and 0.88 mrad were calculated using the formulation given by Born and Wolf.

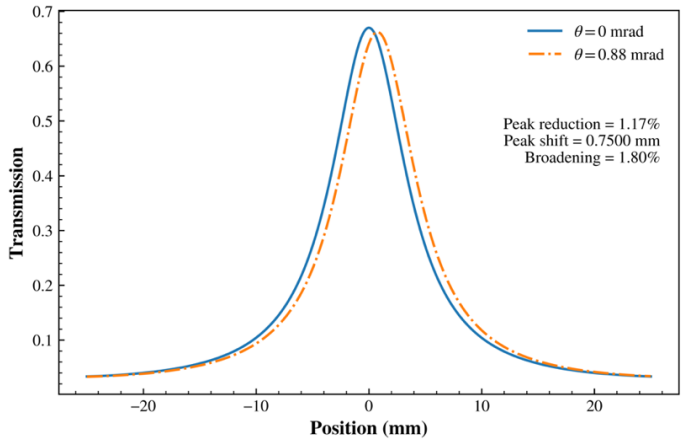


Figure R2. Effect of different divergence angles on the transmission of the Fizeau interferometer.

The calculated transmission curves for divergence half-angles of 0 and 0.88 mrad are shown in Fig. R2. Compared with the case of zero divergence, a divergence half-angle of 0.88 mrad results in only a 1.17% reduction in the peak transmission and a 1.80% increase in the full width at half maximum (FWHM), indicating that the influence of the beam divergence on the shape and width of the Fizeau transmission profile is relatively small. Meanwhile, the transmission peak is shifted by approximately 0.75 mm on the detector plane. Although these effects are limited, the finite divergence angle of the collimated beam was explicitly taken into account in our simulations.

More importantly, in the actual experiment, the receiver transmission profile was experimentally characterized using the same optical configuration as that employed for the atmospheric measurements. Therefore, the measured receiver transmission profile inherently includes the effects associated with the finite divergence angle of the incident beam, including the slight broadening and shift of the transmission fringe. Since this experimentally measured transmission profile is subsequently used in the spectral analysis and atmospheric parameter retrieval, the influence of beam divergence is already incorporated into the receiver response and thus does not introduce an additional unaccounted error in the retrieval.

Comment 9)

Why do you not use the transmission formula of a Fizeau interferometer, as for instance introduced by Born and Wolf?

Response:

Thank you for this comment. The equation used in this study is an angularly averaged Airy transmission function. The Airy function describes the basic Fizeau fringe under the small-shape-factor condition (Mckay, 2002; Vaughan et al., 2025). The integration accounts for the finite angular distribution of the incident beam, assuming a uniform circular angular distribution.

We also apologize for an omission in the original manuscript. A $\sin\theta$ term was inadvertently omitted from Eq. (10). This typographical error has now been corrected

in the revised manuscript.

To verify the validity of this approximation, we calculated the Fizeau interferometer transmission at a beam divergence half-angle of 0.88 mrad using Eq. (10) of the revised manuscript and compared it with that calculated using the Born and Wolf formulation under the same divergence condition. The comparison is presented in Fig. R3 below.

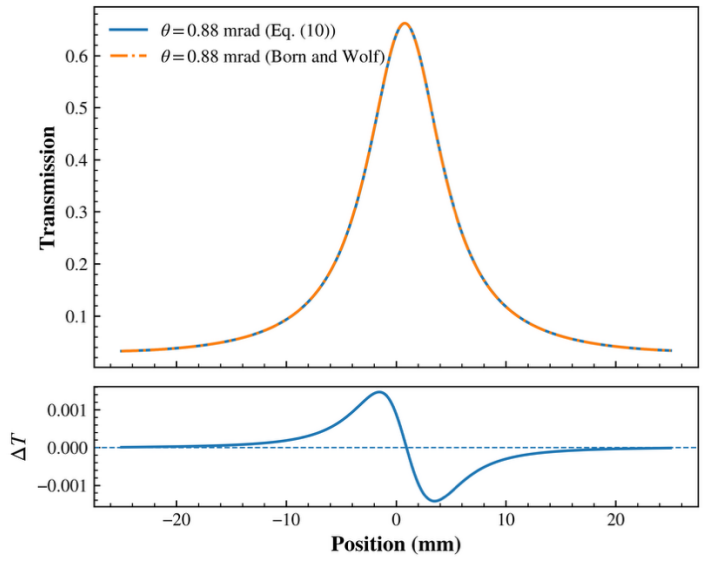


Figure R3. Comparison of the Fizeau interferometer transmission calculated using the Airy function and the Born–Wolf formulation for a divergence half-angle of 0.88 mrad.

Figure R3 compares the Fizeau transmission functions calculated using Eq. (10) and the Born and Wolf formulation at a beam divergence angle of 0.88 mrad. As shown in the upper panel, the two transmission curves almost completely overlap. The lower panel presents their difference, defined as $\Delta T = T_{Eq.\ (10)} - T_{Born\ and\ Wolf}$. The maximum absolute difference is approximately 1.5×10^{-3}, corresponding to only about 0.2% of the peak transmission. The small positive and negative residuals around the fringe peak indicate only a slight difference in fringe asymmetry and position. Therefore, Eq. (10) provides an adequate approximation to the Born and Wolf formulation under the present small-shape-factor condition.

Comment 10)

Have you performed any further numerical simulations to optimize the specifications

of the applied Fizeau interferometer? Or is this a justification that you can use an existing Fizeau interferometer for your test measurements (which would be fine, of course)?

Response:

Thank you for this comment. As explained on Page 9, Lines 205–209, the FSR of the Fizeau interferometer should be between 10 and 12.6 GHz to cover the relevant RB spectrum. An existing three-axis piezoelectrically tunable etalon with a nominal cavity spacing of 12.5 mm was used. The etalon has a free spectral range of approximately 12 GHz at the operating wavelength of 355 nm.

The etalon was initially adjusted to the parallel-plate configuration. The wedge angle required for Fizeau operation was subsequently introduced by varying only the Y-axis piezoelectric actuator, while the X- and Z-axis settings were held at their parallelism values. The differential displacement generated by the Y-axis actuator produces a relative inclination between the two etalon plates. With an effective actuator baseline of 50 mm, the wedge angle is given by:

$$\alpha = \arctan(\frac{\Delta y}{\mathrm{L}})$$

where Δy is the Y-axis displacement relative to the parallel configuration and $\mathrm{L} = 50\ \mathrm{mm}$. The parallel configuration corresponds to a Y-axis digital setting of $N_0 = 33650$. According to the manufacturer, one digital step produces a displacement of approximately 0.1–0.15 nm, and the 16-bit digital interface provides a total adjustment range of 65,535 digital steps, with the Y-axis setting varying from 0 to 65535. Starting from the parallel-plate setting of $N_0 = 33650$, the Y axis can be decreased by 33650 steps or increased by 31885 steps. Using the minimum specified displacement of 0.10 nm per step and an effective actuator baseline of 50 mm, the corresponding wedge angle can be tuned from approximately $-67.3 \sim 63.8\ \mu\mathrm{rad}$.

Therefore, the numerical simulations were not intended to redesign the Fizeau interferometer or to optimize all of its hardware specifications from first principles. Instead, we first demonstrated that the available tunable etalon had a suitable FSR and a sufficient actuator range to operate in the required Fizeau configuration. The

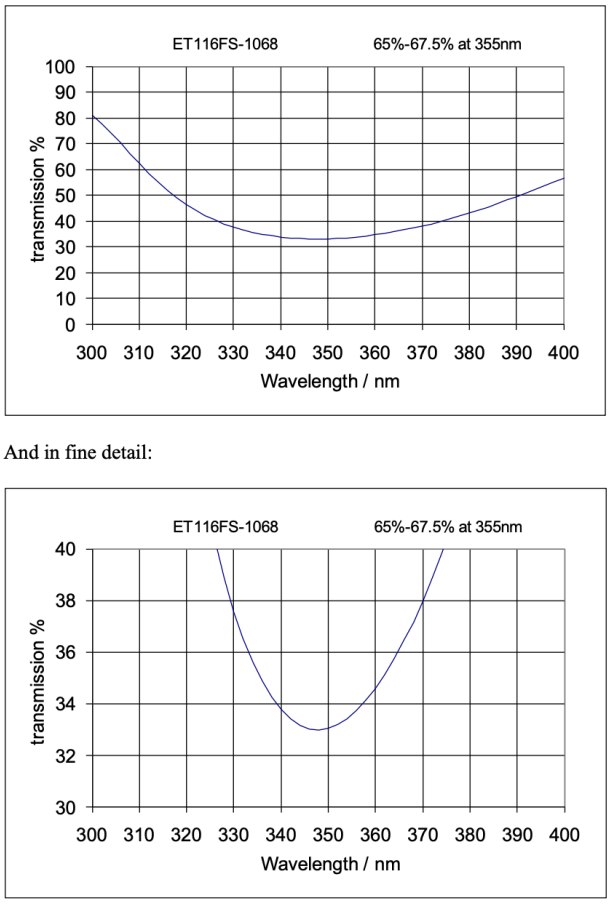
numerical simulations were then used to optimize the operating parameters of this existing device.

Comment 11)

I would expect further important specifications of the Fizeau interferometer to be mentioned here. Especially the mean plate reflectivity as well as the wedge angle that was used.

Response:

Thank you for this comment. The mean plate reflectivity (approximately 66%) at 355 nm and the wedge angle (2.83 µrad) have now been added to Table 2.



And in fine detail:

Figure R4. Measured transmission spectrum of the etalon high-reflectivity coating, with a detailed view shown on an expanded transmission scale

Comment 12)

I do not fully understand the approach or the outcome of this simulation. There is a pretty good estimation of the accuracy for the center and width determination of a Gaussian considering Poisson and white noise (Hagen et al., 2007, https://doi.org/10.1364/AO.46.005374). In this study, it is explained that one needs a certain number of channels (~3) to reach a certain accuracy. When increasing the number of channels, the accuracy does not improve, as the result of each channel gets less accurate (square root of the photons in each channel). Hence, I would expect that you do not see big differences between 32 channels and 64 or 128 channels. Of course, this also depends on the actual fringe shape that you are using, as well as on the conversion factor (channel width and corresponding imaging). I would either suggest clarifying (and checking) these points or maybe skipping this section for this paper, as it is not of primary importance.

Response:

Thank you for this insightful comment. We agree that the previous presentation did not clearly demonstrate how the number of detector channels affects the final retrieval accuracy. In the original manuscript, Fig. 3 showed the Pearson correlation coefficient between the reconstructed and simulated spectra rather than the retrieved temperature and wind errors. This coefficient is affected by both spectral sampling and the signal-to-noise ratio of the individual channels. Consequently, it did not provide a sufficiently direct measure of retrieval performance and made comparison with the expected photon-noise-limited behavior difficult.

We have therefore replaced Fig. 3 with an analysis of the root-mean-square errors (RMSEs) of the retrieved temperature and wind velocity for different detector channel numbers and altitudes, the revised Fig. 3 in manuscript is shown here as Fig. R5. The revised simulations use the same vertical resolution as the atmospheric measurements. At each altitude, the total expected detected photon count and the spectral range are held fixed across the channel configurations. The comparison therefore evaluates the effect of sampling density under the same photon budget.

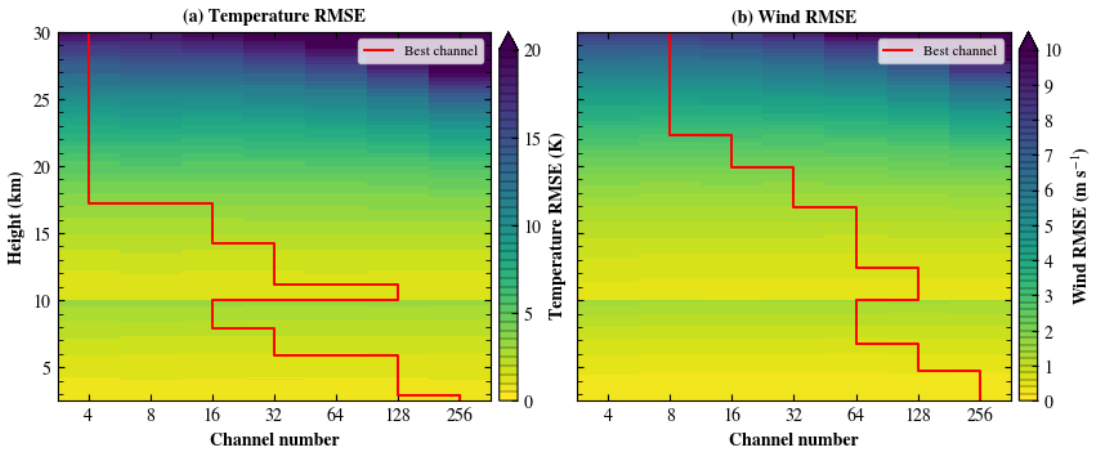


Figure R5. Influence of detector channel number and detection height on the retrieval accuracy of (a) temperature and (b) wind velocity.

Hagen et al. examined the effects of sampling density, finite pixel width, and noise on the estimation of Gaussian spectral parameters, highlighting the importance of balancing spectral sampling resolution and measurement uncertainty (Hagen et al., 2007). As shown in the Fig. R5, increasing the number of channels provides only limited improvement in retrieval accuracy, while configurations with larger numbers of channels may even exhibit degraded performance due to reduced signal-to-noise ratios (SNRs). Ultimately, the 32-channel configuration was selected as a compromise among overall system robustness, complexity, and the commercial availability of multichannel PMT arrays.

The corresponding revisions can be found on Pages 10–11, Lines 244–267.

Comment 13)

I do not understand what is shown here. Do you say that, when analyzing a simulated RB spectrum, your algorithm converges after about one iteration? This makes no sense to me. But maybe I do not understand this figure correctly.

Response:

Thank you for pointing out this ambiguity. We apologize that the definition of "iteration" was not sufficiently clear. Here, one iteration denotes one internal parameter-update step performed by the nonlinear least-squares solver, rather than one complete

execution of the retrieval procedure or one forward-model evaluation. Solver iteration 0 represents the initial parameter deviation.

The original Fig. 5 showed the convergence of the retrieval errors averaged over the simulations at each altitude. However, this averaging obscured the convergence behavior of individual retrievals. To illustrate the process more clearly, Fig. R6 presents one example from the 100 simulation trials, showing the convergence of the retrieved temperature and wind velocity at different altitudes for both large (temperature: +20 K; wind velocity: +20 m s^{-1}; RB amplitude: +50%; Mie amplitude: −50%) and small (temperature: +5 K; wind velocity: +5 m s^{-1}; RB amplitude: +20 %; Mie amplitude: −20%) initial-guess deviations.

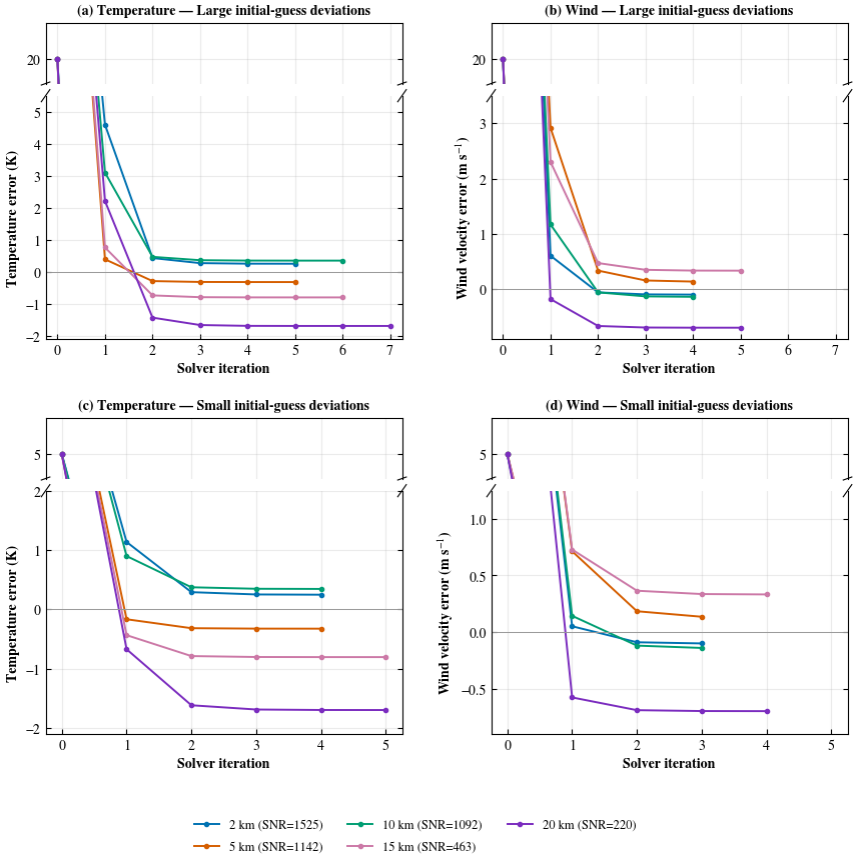


Figure R6. Convergence of temperature and wind velocity retrieval errors at five heights for the first Monte Carlo realization. Iteration 0 denotes initialization.

As shown in Fig. R6, the retrieval errors decrease substantially during the first iteration. However, this initial reduction does not indicate convergence; further iterations are required to refine the parameter estimates and satisfy the convergence criteria.

The revised Fig. 5 in the manuscript summarizes the mean number of iterations required for convergence over the 100 simulation trials, together with the corresponding temperature and wind velocity retrieval results at each altitude, for both large and small initial-guess deviations. For temperature retrieval, the number of iterations increases markedly as the SNR decreases, whereas for wind velocity retrieval, it varies only slightly over the simulated altitude range. Larger initial-guess deviations substantially increase the number of iterations required for convergence. Nevertheless, both initial-guess conditions yield closely consistent final retrievals, indicating that, within the tested conditions, the initial guess affects the convergence speed but has little effect on the converged results. The revised Fig. 5 is shown here as Fig. R7.

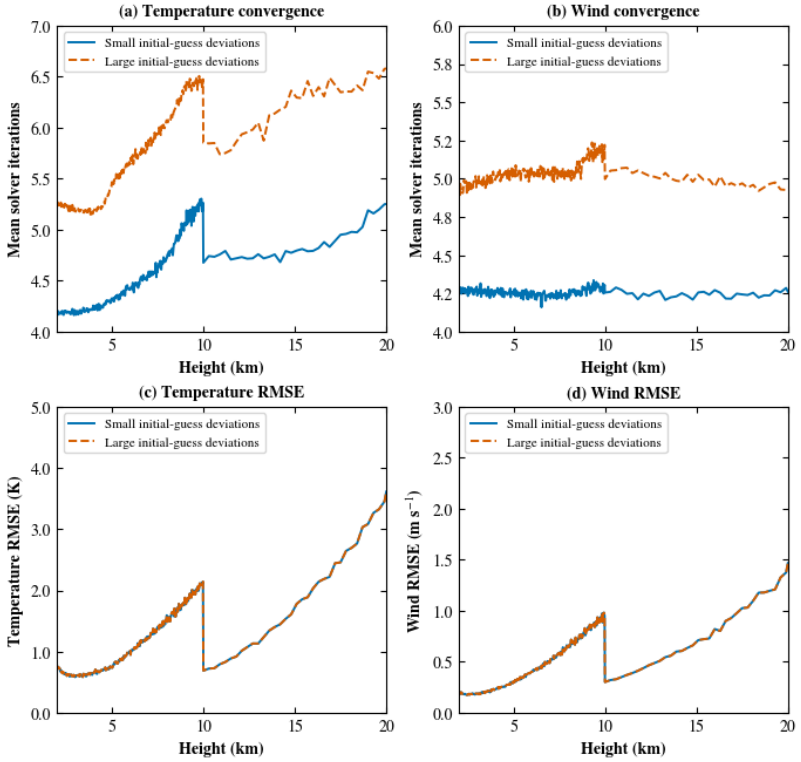


Figure R7. Comparison of mean solver iteration counts for (a) temperature and (b) wind velocity retrievals, and RMSEs of (c) temperature and (d) wind velocity.

The corresponding revisions can be found on page 12–13, lines 279–293 of the revised manuscript.

Comment 14)

It could be helpful to show a few exemplary RB spectra showing how they are used in this simulation, to get a better feeling for what you are analyzing. I would suggest showing both the spectra as well as the best fit, and the corresponding T, p, and Mie that were used for the simulation and retrieved from the fit. With that, the results shown in Fig. 6 could also be much better interpreted.

Response:

Thank you for this helpful suggestion. We have updated Fig. 6 by adding representative simulated photon-count distributions and their best-fit curves at 2 and 15 km. We have also added detailed simulation parameters and examples of the simulated spectra at each altitude to Appendix A.

During this re-examination of the simulations and retrieval implementation, we identified an inappropriate bound on the Mie intensity parameter that restricted its adjustment during fitting. Because temperature and Mie intensity are coupled in the retrieval, this constraint caused the temperature estimate to compensate, leading to an underestimation of temperature. The previously reported bias therefore arose from the parameter constraint in the retrieval implementation, rather than from the prescribed aerosol profile itself. The revised Fig. 6 is shown here as Fig. R8.

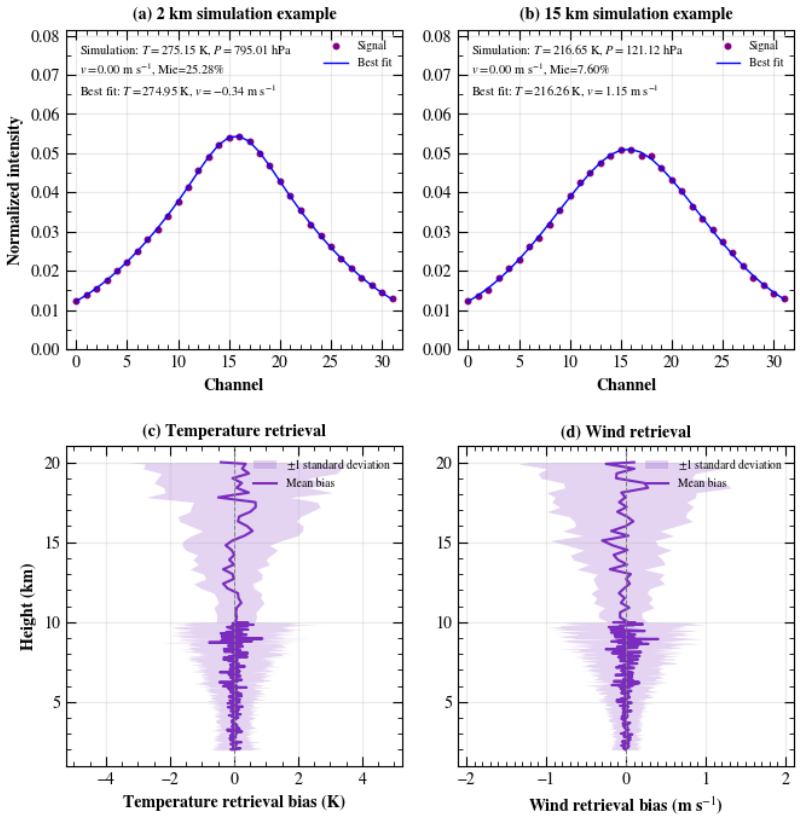


Figure R8. Examples of normalized simulated photon counts and their best fits at (a) 2 km and (b) 15 km. Mean retrieval biases and standard deviations of (c) temperature and (d) wind velocity as functions of height.

The revised results are presented on Pages 13–14, Lines 294–306, and the detailed simulation parameters and example spectra are provided in Appendix A on Page 24.

Comment 15)

For the transmission curve measurement that you show here, it is not clear if you use the same fiber (200 µm, NA = 0.22) that you also use for atmospheric measurements. Furthermore, the fiber illustrates that your imaging setup is defined such that you do not measure down to the "valley" of the transmission curve. This is even less true when the spectrum is convolved with the RB spectrum. This is something I do not understand. Although the edges of the spectrum do not contain many photons, the determination of the valley is important to determine the FWHM of the measured spectrum and hence the temperature. Why do you choose such an imaging configuration? Have you

performed simulations that would justify this approach?

Further, one point that is not discussed in the paper but that is very important is how you transfer the pixel position to a real frequency. Do you have a scannable laser for doing so? How stable is this over time?

Last but not least, the accuracy of the suggested technique significantly depends on a proper correction of the illumination function. How do you perform this correction? How stable is the illumination function over time?

Response:

Thank you for this comment and pointing this out. The transmission-curve calibration was performed using the same multimode fiber employed for the atmospheric measurements (200 μm core diameter and NA = 0.22). Moreover, the position and alignment of the fiber, as well as the entire receiver optical configuration, were kept unchanged between the calibration and atmospheric measurements. We have clarified this point in the revised manuscript.

We agree that sampling the transmission valley can provide useful information for determining the spectral width. However, the temperature in our method is not retrieved by directly measuring the FWHM between the peak and valley. Instead, it is obtained by fitting the complete photon-count distribution recorded by the 32 detector channels using the forward spectral model. The frequency interval represented by each detector channel increases with the Fizeau wedge angle. Therefore, a smaller wedge angle provides finer spectral sampling of the temperature-dependent line shape, although it reduces the total spectral range covered by the detector. To illustrate this trade-off, additional simulations were performed at 15 km using wedge angles of 3, 5, and 10 μrad under otherwise identical conditions. In addition, because a tunable etalon is employed in our receiver, the cavity length along the z-axis can be adjusted to shift the interference pattern, allowing the transmission valley to be experimentally accessed and characterized when required.

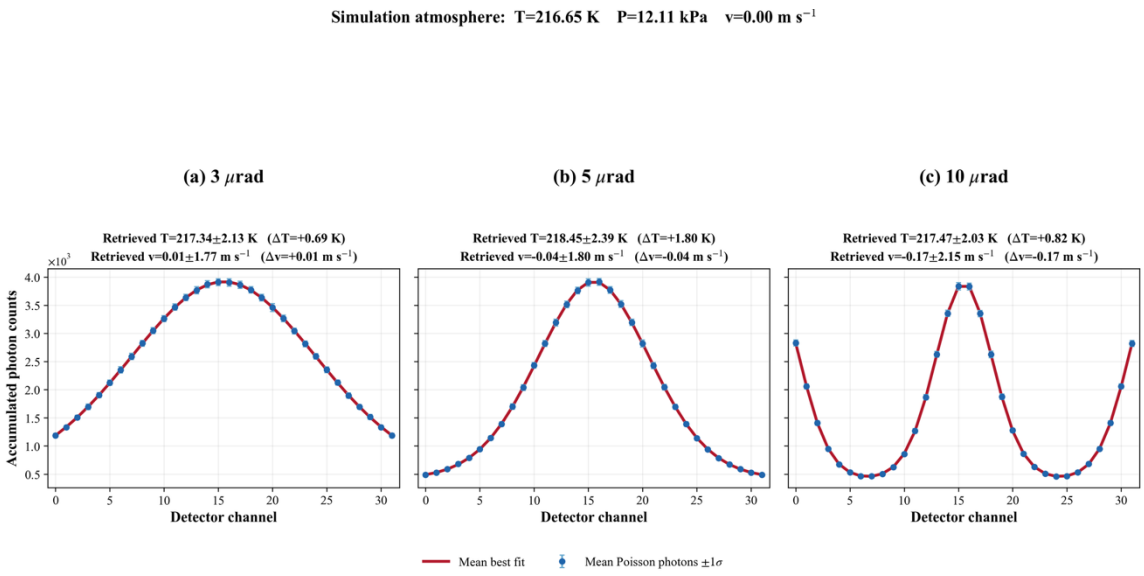


Figure R9. Simulated photon-count distributions and best-fit curves at 15 km for Fizeau wedge angles of (a) 3 μrad, (b) 5 μrad, and (c) 10 μrad.

The input temperature was 216.65 K. Based on 100 independent retrievals with a 5 min accumulation time, the mean retrieved temperatures were 217.34 ± 2.13, 218.45 ± 2.39, and 217.47 ± 2.03 K for wedge angles of 3, 5, and 10 μrad, respectively. The corresponding temperature biases were +0.69, +1.80, and +0.82 K. For an input radial wind speed of 0 m s^{-1}, the retrieved wind speeds were 0.01 ± 1.77, −0.04 ± 1.80, and −0.17 ± 2.15 m s^{-1}, respectively. These results demonstrate that, when retrieval is performed by fitting the complete spectral line shape, the absence of a distinct spectral valley does not adversely affect the retrieval. The fitting algorithm uses the intensity distribution across all detector channels rather than relying on the position or depth of a particular valley. A smaller wedge angle also maps a narrower frequency interval onto each pixel, providing finer spectral sampling. In addition, more returned photons are collected per channel on average, thereby improving the per-channel signal-to-noise ratio. Consequently, the 3 μrad configuration achieved the smallest temperature bias and the lowest wind-speed uncertainty among the three configurations. Under the present simulation conditions, a visible spectral valley is therefore not required for accurate retrieval, and the smaller wedge angle can provide comparable temperature precision and improved wind-speed precision.

The frequency-to-channel response of the receiver was experimentally calibrated using

a tunable continuous-wave laser. During the frequency-scanning experiment, the laser frequency was monitored using a wavelength meter, while the corresponding transmission-peak position on the 32-channel PMT array was determined. The frequency-to-channel conversion factor of 191 MHz channel^{-1} reported in the original manuscript represents the theoretical value calculated from the fitted wedge angle of the Fizeau interferometer and its free spectral range (FSR), rather than the experimentally measured response.

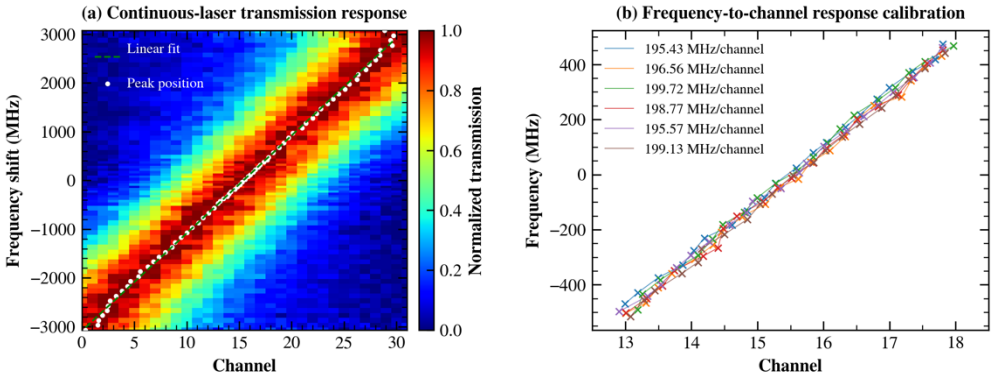


Figure R10. Calibration of the frequency-to-channel response. (a) Measured continuous-wave laser transmission response as a function of detector channel and laser frequency shift. The white dots indicate the fitted peak positions, and the dashed line represents the corresponding linear fit. (b) Frequency-to-channel response obtained from six independent frequency-scanning measurements, with the fitted slopes indicated in the legend (Revised Fig. 9 in manuscript).

To further clarify the experimental calibration, the measured frequency-to-channel response has now been added as Fig. 9 in the revised manuscript. As shown in Fig. R10(a), one frequency scan covered the full response range of the 32-channel detector. A nearly linear relationship between the laser frequency shift and the fitted peak position was observed over most of the detector range. Some deviations from linearity occur near the detector edges (around channels 0 and 31), mainly due to variations in the output energy of the tunable laser during the scan and the limited spectral information available for accurately determining the peak position when the transmission peak approaches the detector boundary.

For the atmospheric wind retrieval, the transmission peak primarily shifts within the central six channels, corresponding approximately to a Doppler-frequency-shift range

of −500 to 500 MHz. Therefore, the frequency-to-channel response was further characterized specifically within this effective working range. Six independent frequency-scanning measurements were performed, as shown in Fig. R10(b), yielding a mean response of 197.53 MHz channel^{-1} with a standard deviation of 1.90 MHz channel^{-1}. This experimentally determined response was used for the subsequent Doppler-frequency-shift determination and wind retrieval. The corresponding description has been added to the revised manuscript on Pages 16–17, Lines 334–358.

The illumination function was calibrated using a broadband LED light source, with the same 200 μm-core, NA = 0.22 multimode fiber that was used for the atmospheric measurements. The corresponding description has also been added to Pages 14–15, Lines 309–318 of the revised manuscript. The revised Fig. 7 is shown here as Fig. R11.

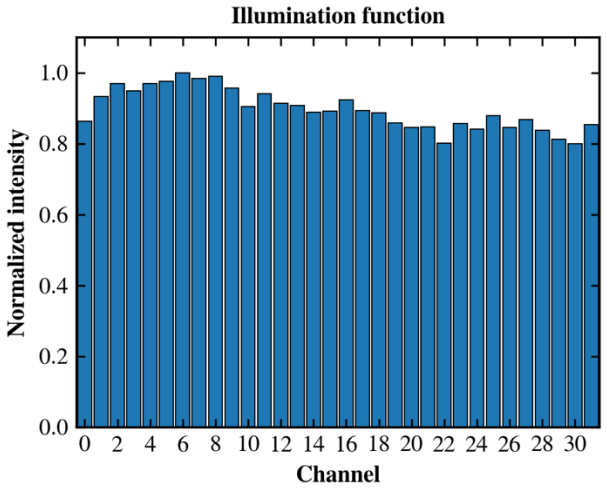


Figure R11. Illumination function of the 32-channel PMT array.

Before each atmospheric observation, the Fizeau transmission response was measured using the same pulsed laser employed for the atmospheric measurements. The repeatability of these measurements provides an indirect indication of the stability of the overall receiver response, including the illumination function.

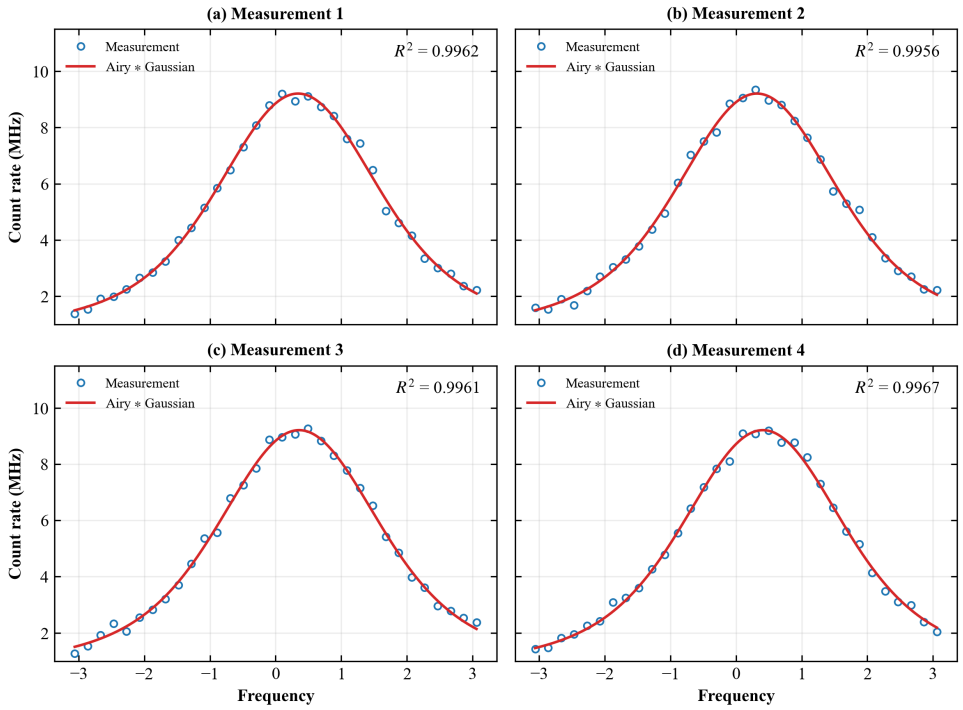


Figure R12. Receiver calibration results.

As shown in Fig. R12, the measured receiver responses exhibit good repeatability, indicating that the overall receiver response remained relatively stable under the tested conditions. This also provides indirect evidence that the illumination function was relatively stable.

Comment 16)

This figure actually illustrates the point I mentioned above. The measured raw signal does not reach the valleys. Furthermore, the shown spectrum is pretty asymmetric. I do not understand how you can retrieve such precise temperature and wind values from this raw signal. Could you clarify that? Could you show the best fit to these particular spectra and the fit values that you retrieve? Is the blue curve the best fit to the purple data points? If so, I think there must be something wrong. With such poor agreement, it should be impossible to derive correct parameters. But maybe I do not understand this correctly here.

Response:

Thank you for raising this important and constructive point. The issue that the measured

spectrum does not extend to the transmission valleys has been addressed in our response to Comment 15.

Regarding the apparent asymmetry, first, the spectral center does not coincide with the central channel of the PMT array, and therefore the measured spectral distribution is not expected to be symmetric with respect to the center of the detector. Second, the purple data points in the original figure represent the completely raw measured signal, without correction for the illumination function. Therefore, the nonuniform illumination distribution can contribute to the apparent asymmetry of the raw spectrum. Before retrieving the atmospheric parameters, the raw signal is corrected using the illumination function, as described in our response to Comment 15. We have revised the figure to show the illumination-corrected signal and updated the corresponding caption to make this processing step explicit and avoid ambiguity.

We also apologize that the meaning of the blue curve was not sufficiently clear. In the original figure, it represented the atmospheric scattering spectrum obtained after deconvolving the measured receiver response, rather than the best-fit curve to the purple data points. In the revised figure, we have replaced this deconvolved spectrum with the best-fit curve to the measured signal and included the retrieved parameter values, allowing the agreement between the measurement and the fit to be assessed directly. The revised Fig. 10 is shown here as Fig. R13.

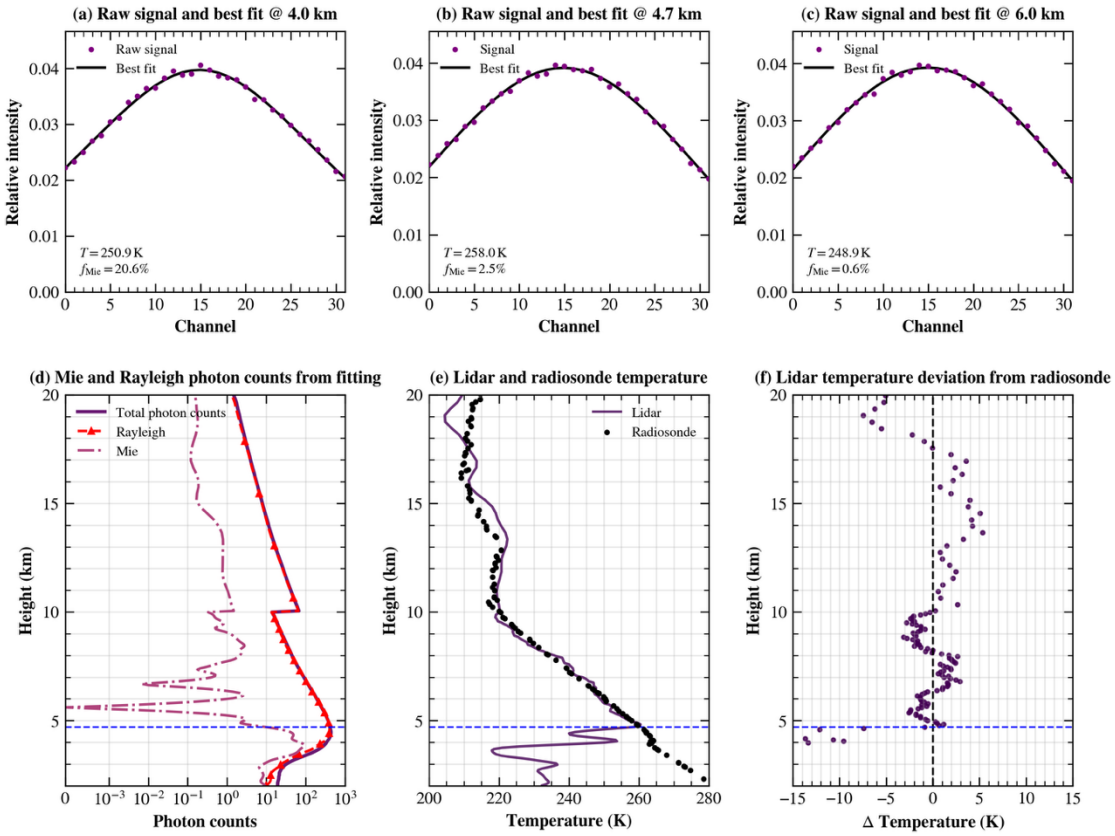


Figure R13. Spectral fitting results and evaluation of the influence of Mie scattering on temperature retrieval. (a–c) Best-fitting results of the measured signals at 4.0, 4.7, and 6.0 km. (d) Retrieved total, RB, and Mie photon counts. (e) Comparison between the lidar-retrieved and radiosonde temperature profiles. (f) Temperature difference (lidar minus radiosonde). The blue dashed line indicates the lower boundary of the temperature retrieval (4.7 km).

The revised figure is presented as Fig. 10 on Page 17.

Comment 17)

I do understand that the temperature retrieval is significantly impacted by Mie scattering, but the wind retrieval shouldn't be. As it is "just" a determination of the fringe position, this should also work in the vicinity of Mie scattering. Actually, it should even provide better results due to the higher signal levels. Could you clarify that? The wind profiles start already at 2 km but do not go down to the ground. Is this related to overlap issues?

Can you show further spectra for cloud returns and from the free atmosphere for comparison? Also, could you show the best-fit result? It is also not clear how you

retrieve the wind. What is your reference?

Response:

Thank you for this insightful comment. We agree with the reviewer that, unlike temperature retrieval, which is sensitive to the spectral shape and can therefore be significantly affected by enhanced Mie scattering, wind retrieval mainly relies on the determination of the spectral center. Therefore, enhanced Mie scattering does not fundamentally prevent wind retrieval and may even improve the statistical precision due to the increased signal level. We have revised the manuscript accordingly to clarify this point on Page 21, Lines 413-424. In addition, we have further clarified that the radiosonde launch site was located approximately 100 km from the lidar observation site, this information has been added to the revised manuscript on Page 19, Line 393. The relatively large wind-speed deviations observed at lower altitudes may therefore partly arise from spatial inhomogeneity in the tropospheric wind field, as the lidar and radiosonde sampled the atmosphere at different locations.

Regarding the lower limit of the wind profiles, the lidar system employs a bistatic transmitter–receiver configuration. In the near-field region, the transmitted laser beam and the receiver field of view do not geometrically overlap, preventing reliable wind retrieval down to the ground. This limitation has been clarified in the revised manuscript on Page 18, Lines 387–388.

To provide a more direct comparison, we have added representative measured spectra from a cloud-affected region and from the free atmosphere. Fig. R14 shows the measured spectra and the corresponding best-fit results at approximately 5 km and 10 km.

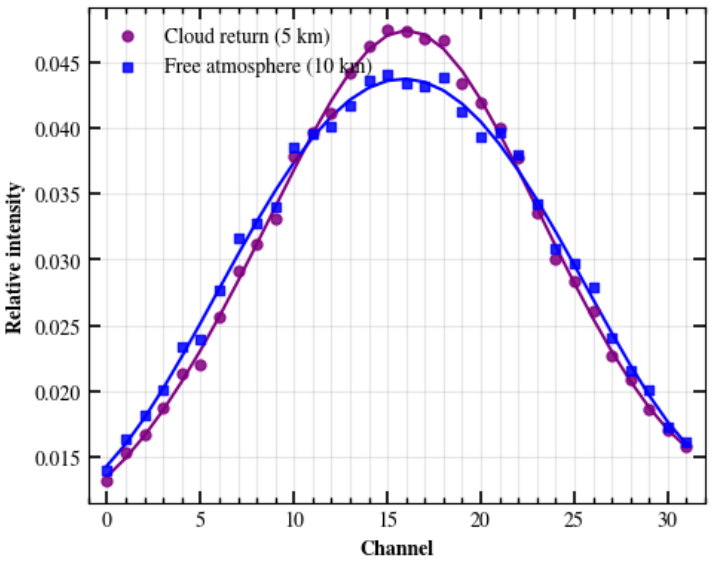


Figure R14. Measured spectra and corresponding best-fit results for a cloud-affected return at 5 km and a free-atmospheric return at 10 km.

The laser frequency was continuously monitored by a wavelength meter during the atmospheric measurements, providing a real-time reference for the transmitted laser frequency. Since our system operates as a scanning Doppler wind lidar, measurements were performed in opposite viewing directions. The wind component was then derived from the difference between the Doppler velocities measured in the two opposite directions. In this way, common systematic frequency offsets are largely cancelled, while the atmospheric Doppler contribution changes sign and is retained. We have clarified the wind retrieval procedure and its frequency reference in the revised manuscript on Page 20, Lines 403–408. The Doppler velocities retrieved for the individual viewing directions before the opposite-direction subtraction are shown in Fig. R15.

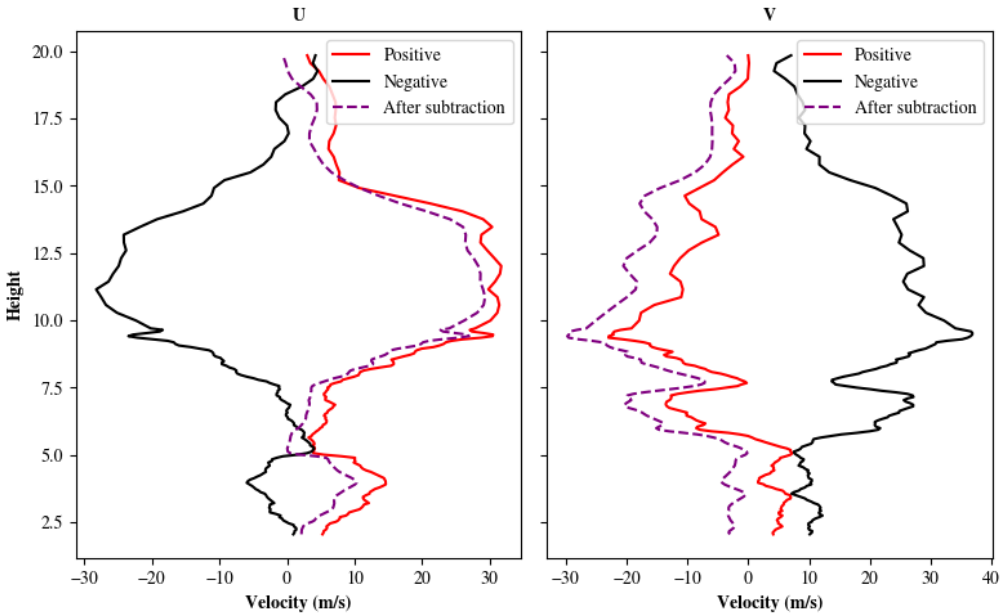


Figure R15. Opposing-direction measurements of the lidar-derived U and V wind components.

References in this response:

Hagen, N., Kupinski, M., and Dereniak, E. L.: Gaussian profile estimation in one dimension, Applied Optics, 46, 5374-5383, 10.1364/AO.46.005374, 2007.

McKay, J. A.: Assessment of a multibeam Fizeau wedge interferometer for Doppler wind lidar, Applied Optics, 41, 1760-1767, 10.1364/AO.41.001760, 2002.

Vaughan, M., Ridley, K., Witschas, B., Lux, O., Nikolaus, I., and Reitebuch, O.: Spectral performance analysis of the Fizeau interferometer on board ESA's Aeolus wind lidar satellite, ATMOSPHERIC MEASUREMENT TECHNIQUES, 18, 2149-2181, 10.5194/amt-18-2149-2025, 2025.

Witschas, B.: Analytical model for Rayleigh–Brillouin line shapes in air, Applied Optics, 50, 267-270, 10.1364/AO.50.000267, 2011a.

Witschas, B.: Analytical model for Rayleigh–Brillouin line shapes in air: errata, Applied Optics, 50, 5758-5758, 10.1364/AO.50.005758, 2011b.

Witschas, B., Vieitez, M. O., van Duijn, E.-J., Reitebuch, O., van de Water, W., and Ubachs, W.: Spontaneous Rayleigh–Brillouin scattering of ultraviolet light in nitrogen, dry air, and moist air, Applied Optics, 49, 4217-4227, 10.1364/AO.49.004217, 2010.